
SUBQUAD: NEAR-QUADRATIC-FREE STRUCTURE INFERENCE WITH DISTRIBUTION-BALANCED OBJECTIVES IN ADAPTIVE RECEPTOR FRAMEWORK

Rong Fu*
 University of Macau
 mc46603@um.edu.mo

Zijian Zhang
 University of Pennsylvania
 zzjharry@alumni.upenn.edu

Wenxin Zhang
 University of Chinese Academy of Sciences
 zwxzhang12@163.com

Kun Liu
 University of Southampton
 kundy9909@gmail.com

Jiekai Wu
 Juntendo University
 ketsu0612@gmail.com

Xianda Li
 University of Bologna
 xianda.li@studio.unibo.it

Simon Fong
 University of Macau
 ccfong@um.edu.mo

February 20, 2026

ABSTRACT

Comparative analysis of adaptive immune repertoires at population scale is hampered by two practical bottlenecks: the near-quadratic cost of pairwise affinity evaluations and dataset imbalances that obscure clinically important minority clonotypes. We introduce **SubQuad**, an end-to-end pipeline that addresses these challenges by combining antigen-aware, near-subquadratic retrieval with GPU-accelerated affinity kernels, learned multimodal fusion, and fairness-constrained clustering. The system employs compact MinHash prefiltering to sharply reduce candidate comparisons, a differentiable gating module that adaptively weights complementary alignment and embedding channels on a per-pair basis, and an automated calibration routine that enforces proportional representation of rare antigen-specific subgroups. On large viral and tumor repertoires SubQuad achieves measured gains in throughput and peak memory usage while preserving or improving recall@k, cluster purity, and subgroup equity. By co-designing indexing, similarity fusion, and equity-aware objectives, SubQuad offers a scalable, bias-aware platform for repertoire mining and downstream translational tasks such as vaccine target prioritization and biomarker discovery.

Keywords Representation Learning, Immunoinformatics, Fairness, Hardware Acceleration, Visual Analytics, Graph Representation Learning, Metric Learning, Biological Networks

1 Introduction

An immune repertoire denotes the complete collection of T cell receptor (TCR) and B cell receptor (BCR) sequences within an individual. These repertoires constitute the adaptive immune system's molecular fingerprint and commonly comprise millions to hundreds of millions of distinct receptor sequences. Comparing repertoires across individuals or clinical states can reveal antigen-specific response patterns that inform vaccine design, guide cancer immunotherapy strategies and support monitoring of autoimmune disease. Such comparative analyses are therefore routinely needed in translational immunology yet face acute computational constraints: pairwise affinity evaluations grow quadratically

*Corresponding author: mc46603@um.edu.mo

with the number of sequences, and naive comparison becomes infeasible for modern datasets containing 10^6 – 10^7 sequences per donor.

Prior work has addressed parts of this scalability challenge through algorithmic and engineering advances. Locality-sensitive hashing and MinHash variants provide subquadratic heuristics for candidate reduction [1, 2], while accelerator-optimized kernels and specialized hardware have been used to speed low-level similarity computations [3, 4]. Despite these gains, three practical limitations remain. First, many scalable pipelines process receptor sequences as generic strings and consequently discard antigen-relevant signals important for epitope binding. Second, subgroup representation has received limited consideration, which risks systematic omission of low-prevalence but clinically consequential clonotypes. Third, verifiability of runtime and memory claims is often undermined by incomplete reporting of index and kernel configuration details.

From a translational standpoint, correcting subgroup imbalance is not merely an abstract fairness objective but a domain requirement. Rare antigen-specific clonotypes, including those reactive to uncommon viral variants or tumor neoantigens, may occur at very low frequency while nevertheless driving clinically meaningful responses. Pipelines that optimize only for aggregate speed or for dominant patterns are therefore liable to underrepresent these high-value minorities, biasing downstream tasks such as epitope prioritization and biomarker selection. Incorporating equity-oriented penalties into retrieval and clustering objectives helps preserve representation for rare but important groups and thereby improves the biological validity of subsequent analyses.

Motivated by these challenges, we propose **SubQuad**, a end-to-end pipeline for scalable, antigen-aware, and equity-preserving analysis of large immune repertoires. SubQuad integrates three key innovations: an antigen-aligned MinHash retrieval module that combines repertoire-specific sketching with biologically guided blocking to achieve near-subquadratic candidate reduction while maintaining high recall; a multimodal fusion backbone with a differentiable gating controller that adaptively combines alignment signals, protein-language embeddings, and local graph features to capture both fine-grained edits and higher-level biochemical structure; and a fairness-aware spectral clustering objective with automated equity calibration to ensure proportional representation of rare antigen-specific clonotypes and reduce subgroup disparity.

Our primary contributions are summarized as follows. First, we introduce **SubQuad**, an end-to-end framework that couples high-efficiency sequence retrieval with antigenic sensitivity, enabling the construction of large-scale immune repertoire graphs without the quadratic cost of exhaustive comparisons. Second, we develop a dual-phase meta-learning encoder and a learnable similarity fusion backbone that dynamically integrates alignment-based and embedding-based affinities to support robust clonotype-to-phenotype modeling. Third, we formulate an explicit, equity-constrained clustering objective combined with an automated calibration routine, ensuring that rare but clinically significant antigen-specific subgroups are preserved across diverse repertoire topologies. Extensive evaluations on viral and cancer repertoires demonstrate substantial gains in runtime, memory efficiency, and biological fidelity, while ablation studies confirm that antigen-aligned blocking and multimodal fusion are critical for maintaining high cluster purity and fairness. Together, these components transform repertoire comparison into a scalable and biologically valid graph-learning task, providing a practical foundation for epitope prioritization, biomarker discovery, and vaccine design.

2 Related Work

We summarize related work in five areas: scalable retrieval, sequence representation, graph-based repertoire modeling, fairness-aware clustering, and systems–biology integration.

2.1 Scalable retrieval.

MinHash and locality-sensitive hashing reduce pairwise comparisons in high-dimensional spaces [1]. Practical performance depends on index design and hardware use, as shown in FAISS, HNSW, and ScaNN [5, 6]. Bioinformatics systems combine sketching with graph search or GPU acceleration for genome-scale data [7, 8, 9, 10]. SubQuad extends this by integrating antigen-aware alignment with GPU-parallel MinHash kernels.

2.2 Sequence representation.

Protein and nucleotide language models yield embeddings that complement alignment-based similarity [11, 12, 13]. Fusion mechanisms with learnable gating combine heterogeneous signals [14, 15, 16, 17]. SubQuad applies a gating network to integrate alignment, embedding, and graph context.

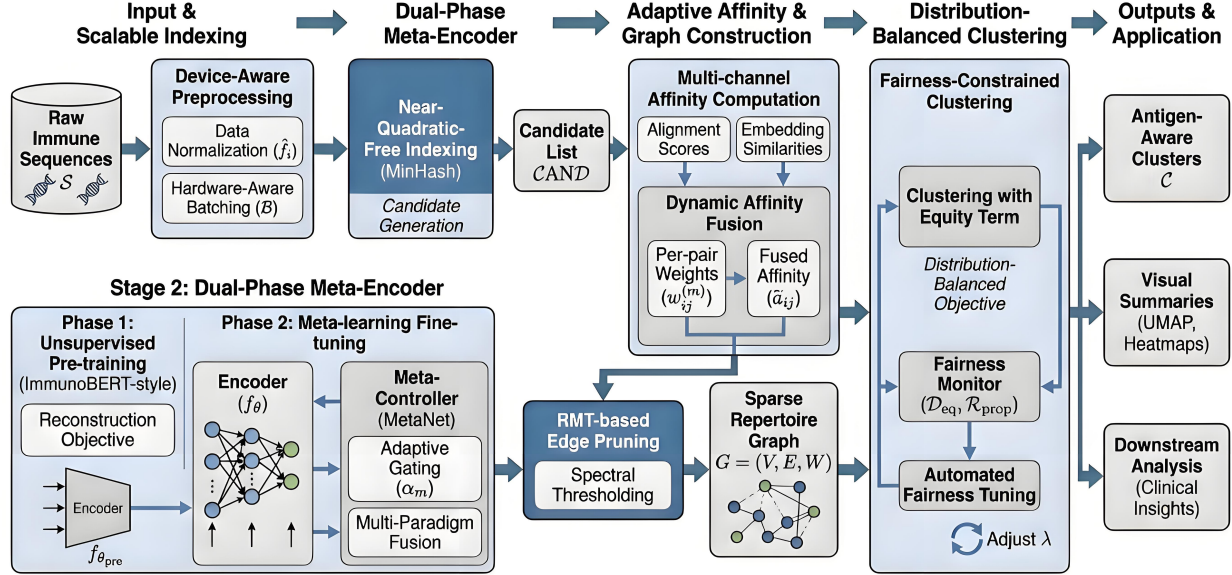


Figure 1: Overview of the **SubQuad** framework for near-quadratic-free, equity-aware repertoire inference. **Scalable Preprocessing:** Raw sequences \mathcal{S} are processed via **MinHash-based Indexing** to generate a sparse candidate list \mathcal{CAND} and optimized using hardware-aware batching \mathcal{B} . **Representation Learning:** A **Dual-Phase Meta-Encoder** utilizes **ImmunoBERT**-style pretraining followed by **MetaNet** fine-tuning. The **Meta-Controller** dynamically adjusts gating weights α_m for multi-paradigm fusion. **Graph Construction:** Multi-channel affinities are integrated via **Dynamic Affinity Fusion** to produce \tilde{a}_{ij} . This similarity matrix is refined through **RMT-based Thresholding** (eigenvalue spectrum analysis) to produce a sparse weighted graph $G = (V, E, W)$. **Fairness-Constrained Clustering:** The graph is partitioned into clusters \mathcal{C} by optimizing a joint objective of spatial cohesion and **Jensen-Shannon Equity**. An **Automated Fairness Tuner** dynamically calibrates the trade-off weight λ to meet target disparity δ_{max} . **Outputs:** The pipeline yields antigen-aware clusters, topological maps (UMAP), and equity heatmaps for clinical interpretation.

2.3 Graph-based repertoire modeling.

Similarity graphs reveal immune community structure and functional modules [18, 19]. Spectral methods and graph neural networks support antigenic neighborhood detection. SubQuad uses a spectral-style pipeline with group-aware penalties to balance coherence and representation.

2.4 Fairness-aware clustering.

Fairness methods include proportional representation, constrained optimization, and pairwise regularization [20, 21, 22, 23]. Extensions to relational graphs preserve structure while enforcing group-level guarantees [24]. Biomedical applications require attention to sampling bias and underrepresented groups [25, 26]. SubQuad adapts these tools with disparity measures and automated fairness tuning.

2.5 Systems-biology integration.

High-throughput analysis benefits from coordinated design of indexing, compute kernels, and workflows [3, 4, 8]. FAIR workflows promote transparency and reuse [27, 28]. SubQuad combines efficient indexing, GPU affinity kernels, and biologically informed fusion and fairness modeling with documented configurations for benchmarking.

3 Methodology

We introduce **SubQuad**, an end-to-end pipeline for accelerated, equity-aware representation learning on large immune-repertoire graphs. SubQuad is built around three practical components. The first is device and memory aware preprocessing and indexing, which stabilizes large-scale runs and reduces the number of candidate comparisons. The second is a dual phase meta-learning encoder that incorporates a learnable, dynamic multi channel fusion backbone to

support robust clonotype to phenotype modeling. The third is a fairness constrained clustering module that includes an automated calibration routine for selecting fairness weights. Our implementation adapts and extends protein language model embeddings inspired by ImmunoBERT [12] as well as a high-performance correlation and network-analysis toolkit inspired by MetaNet [29]; these components have been modified for repertoire-scale workloads and are not used verbatim. MetaNet is a lightweight meta-controller that dynamically fuses alignment-derived scores with embedding-based similarities by learning pair-specific gating weights, enabling adaptive integration of complementary affinity signals without introducing task-specific heuristics.

The SubQuad framework integrates system-level efficiency with biological fidelity. To compare immune repertoires at scale, we utilize a repertoire-level distance measure that quantifies divergence through cluster-mass distributions and graph edit operations as detailed in Appendix A. This structural representation is supported by a GPU-optimized parallel computing architecture described in Appendix F, which leverages a two-dimensional grid organization to handle large-scale memory hierarchies. Central to our approach is the fairness-constrained optimization framework. We move beyond conventional statistical parity to ensure that rare but clinically significant antigen-specific clonotypes are not overlooked. The mathematical formulation of this objective, which balances clustering cohesion with subgroup equity, is provided in Appendix E. Furthermore, we address the inherent limitations of standard divergence measures in long-tailed biological distributions. A formal discussion on the necessity of our fairness objective is available in Appendix G, while Appendix D.1 provides a theoretical proof (Theorem D.1) regarding the coverage lower bounds for rare subgroups.

3.1 Task Formalisation: Antigen-Aware Repertoire Graph Construction

$$\mathcal{T} : \mathcal{S} \mapsto G \quad (1)$$

where $\mathcal{S} = \{s_i\}_{i=1}^n$ denotes a collection of immune receptor sequences sampled from a repertoire, and $G = (V, E, W)$ is the resulting sparse weighted graph whose vertices V correspond to individual sequences, edges E encode antigen-driven similarity links, and edge weights $W = \{w_{ij}\}$ quantify the antigen-level resemblance between sequence pairs (s_i, s_j) .

3.2 Dual-phase meta-learning encoder

We train the representation backbone in two consecutive stages. The first stage performs unsupervised representation pretraining via a reconstruction objective:

$$\min_{\theta_{\text{pre}}} \mathcal{L}_{\text{recon}}(f_{\theta_{\text{pre}}}(X), X). \quad (2)$$

where $f_{\theta_{\text{pre}}}(\cdot)$ denotes the encoder used for representation learning, θ_{pre} are the encoder parameters, and X denotes the set of inputs used for reconstruction pretraining.

After pretraining we fine-tune the encoder jointly with a lightweight meta-network and a downstream task head:

$$\min_{\theta_{\text{pre}}, \theta_{\text{meta}}} \mathcal{L}_{\text{task}}(\text{MetaNet}_{\theta_{\text{meta}}} \circ f_{\theta_{\text{pre}}}(X), Y), \quad (3)$$

where $\text{MetaNet}_{\theta_{\text{meta}}}(\cdot)$ denotes the meta-controller applied to encoder outputs, θ_{meta} denotes its parameters, the operator “ \circ ” denotes functional composition, and Y denotes downstream supervision signals or task labels.

To accelerate convergence we employ momentum-style updates:

$$\theta_{t+1} = \theta_t - \eta_t \nabla_{\theta} \mathcal{L}(\theta_t) + \mu_t (\theta_t - \theta_{t-1}), \quad (4)$$

where η_t denotes the learning rate at iteration t and μ_t denotes the momentum coefficient (in practice we typically set $\mu_t \approx 0.9$).

3.3 Architectural components

Adaptive channel weighting. We compute a compact per-channel importance score for each modality m :

$$\alpha_m = \sigma(\mathbf{W}_{\text{meta}} \mathbf{F}_m + \mathbf{b}_{\text{meta}}), \quad (5)$$

where α_m is the importance weight assigned to channel m , \mathbf{F}_m is the feature tensor for channel m , \mathbf{W}_{meta} and \mathbf{b}_{meta} are learnable parameters of the meta-scoring layer, and $\sigma(\cdot)$ is the sigmoid activation function.

Topology-aware graph propagation. We propagate node features with a normalized aggregation rule:

$$h_v^{(k+1)} = \text{ReLU} \left(\sum_{u \in \mathcal{N}(v)} \frac{\mathbf{W}^{(k)} h_u^{(k)}}{\sqrt{|\mathcal{N}(v)|} \sqrt{|\mathcal{N}(u)|}} \right). \quad (6)$$

where $h_v^{(k)}$ denotes node v 's representation after k propagation steps, $\mathcal{N}(v)$ denotes the neighborhood of node v , and $\mathbf{W}^{(k)}$ is the layer-specific linear transform applied at propagation step k .

Prototype-contrastive consolidation. To concentrate representation mass for rare clonotypes we maintain class prototypes and optimize a prototype-centered contrastive loss:

$$\mathbf{p}_c = \frac{1}{|\mathcal{S}_c|} \sum_{x \in \mathcal{S}_c} f_\theta(x), \quad (7)$$

$$\mathcal{L}_{\text{proto}} = - \sum_{x \in \mathcal{B}} \log \frac{\exp(\langle f_\theta(x), \mathbf{p}_{y(x)} \rangle / \tau)}{\sum_{c' \in \mathcal{N}_x} \exp(\langle f_\theta(x), \mathbf{p}_{c'} \rangle / \tau)}. \quad (8)$$

where \mathbf{p}_c denotes the prototype vector for class c , \mathcal{S}_c denotes the set of examples with label c , $f_\theta(\cdot)$ denotes the instance embedding function parameterized by θ , \mathcal{B} denotes the training batch, $y(x)$ denotes the class label of instance x , $\tau > 0$ is the temperature hyperparameter, and \mathcal{N}_x denotes the set of negative prototypes considered for x .

Multi-paradigm fusion. We fuse channel outputs via element-wise gated aggregation:

$$\mathbf{F}_{\text{fusion}} = \sum_{m=1}^M \alpha_m \odot \text{LayerNorm}(\mathbf{F}_m), \quad (9)$$

with LayerNorm defined by

$$\text{LayerNorm}(x) = \gamma \frac{x - \mu}{\sqrt{\sigma^2 + \epsilon}} + \beta. \quad (10)$$

where $\mathbf{F}_{\text{fusion}}$ denotes the fused multi-channel representation, α_m are the channel gating scalars from Eq. (5), \odot denotes element-wise multiplication, γ and β are learnable scale and shift parameters, μ and σ^2 denote the mean and variance computed along the normalization axis, and $\epsilon > 0$ is a small constant for numerical stability.

3.4 Data normalization and hardware-aware batching

We apply conservative imputations for sparse frequency data:

$$\hat{f}_i = \text{median}(\{f_j\}_{j=1}^n), \quad (11)$$

where $\{f_j\}_{j=1}^n$ are the observed clone frequencies for the dataset and \hat{f}_i denotes the imputed frequency assigned to item i .

Batch size is chosen to respect device memory limits:

$$\mathcal{B} = \min \left(|\mathcal{S}|, \max \left(32, \left\lfloor \sqrt{\frac{\mathcal{M}_{\text{avail}}}{c \cdot \ell_{\text{max}}}} \right\rfloor \right) \right), \quad (12)$$

where $|\mathcal{S}|$ denotes the number of sequences available in the current epoch, $\mathcal{M}_{\text{avail}}$ denotes available memory in bytes on the compute device, ℓ_{max} denotes the maximum sequence length considered, and c denotes a per-sequence memory overhead constant.

3.5 Overview: end-to-end algorithm

Algorithm 1 SubQuad (End-to-End Pipeline)

Require: Raw sequences \mathcal{S} , optional subgroup labels \mathcal{G} , target disparity δ_{\max}

Ensure: Clusters \mathcal{C} , graph G , visual summaries

Preprocessing:

- 1: Trim/pad sequences, compute MinHash sketches, extract metadata.
- 2: Build antigen-aware MinHash index; generate candidate list \mathcal{CAND} for each query.

▷ see Sec. 3.4

Embedding:

- 3: **for** each $x \in \mathcal{S}$ **do**
- 4: Compute embedding \mathbf{v}_x using modified ImmunoBERT encoder.
- 5: Optionally apply momentum-style parameter updates (Eq. (4)).
- 6: **end for**

▷ Eqs. (2), (3)

Affinity Computation:

- 7: **for** each candidate pair $(i, j) \in \mathcal{CAND}$ **do**
- 8: Compute multi-channel affinities $\{a_{ij}^{(m)}\}_{m=1}^M$.
- 9: Compute scoring $g^{(m)}(x_i, x_j)$ and weights $w_{ij}^{(m)}$ via Eq. (13).
- 10: Fuse affinities to obtain \tilde{a}_{ij} via Eq. (14).
- 11: **end for**

▷ Eqs. (7), (8)

Graph Construction:

- 12: Construct similarity matrix $A = [\tilde{a}_{ij}]$ (see Eq. (14)).
- 13: Apply RMT-based eigenvalue thresholding to $A \rightarrow G = (V, E, W)$.

Fair Clustering:

- 14: Run fairness-constrained clustering on G (Eq. (15)).
- 15: Evaluate disparity measures (Eqs. (16)–(17)).
- 16: Tune λ with automated fairness tuner (see Sec. 3.9) to meet δ_{\max} .

Post-processing & Outputs:

- 17: Generate visual summaries (UMAP, topological maps, disparity heatmaps).
- 18: **return** \mathcal{C}, G , and visual summaries.

As shown in Algorithm 1, the SubQuad pipeline operates in an end-to-end manner.

3.6 Dynamic affinity fusion (per-pair)

We benchmark SubQuad on three complementary missions: retrieving antigen-enriched neighbours at the sequence level, surfacing rare clonotype clusters across repertoires, and furnishing interactive UMAP and topological maps that clinicians can interrogate without prior machine-learning expertise. Let $\{a_{ij}^{(m)}\}_{m=1}^M$ denote affinity channels computed for sequence pair (i, j) . We compute soft channel scores $g^{(m)}(x_i, x_j)$ and normalize them into per-pair weights:

$$w_{ij}^{(m)} = \frac{\exp(g^{(m)}(x_i, x_j))}{\sum_{m'=1}^M \exp(g^{(m')}(x_i, x_j))}, \quad (13)$$

$$\tilde{a}_{ij} = \sum_{m=1}^M w_{ij}^{(m)} a_{ij}^{(m)}. \quad (14)$$

where $a_{ij}^{(m)}$ denotes the affinity score from channel m for pair (i, j) , $g^{(m)}(\cdot, \cdot)$ denotes the small scoring network (e.g., a two-layer MLP) that outputs an unnormalized relevance for channel m , $w_{ij}^{(m)}$ are the normalized per-pair channel weights from Eq. (13), and \tilde{a}_{ij} denotes the fused affinity used to populate the similarity matrix.

3.7 Graph construction and RMT-based thresholding

We construct a symmetric similarity matrix $A = [\tilde{a}_{ij}]$. To suppress spurious correlations we employ a random-matrix-theory (RMT) inspired thresholding procedure. Concretely, we compute the eigenvalue spectrum of A , estimate the bulk cutoff from that spectrum, and remove edges whose weights fall below the resulting data-driven threshold. The output is a sparse weighted graph $G = (V, E, W)$. Here V denotes the set of nodes, namely sequences, E denotes the set of edges retained after thresholding, and W denotes the associated edge weights.

3.8 Fairness-constrained clustering

Immunological motivation. Immune repertoires are highly imbalanced. Rare antigen-specific subgroups, although infrequent, can play critical clinical roles, for example clones that respond to rare pathogens or tumor neoantigens. Clustering methods that emphasize only abundant patterns may overlook these important minorities, which can create blind spots in vaccine or therapy design. To address this challenge, we introduce an explicit equity term into the clustering objective so that biologically meaningful but low-frequency subgroups remain adequately represented for reliable downstream analysis. Since the JS-divergence fairness term may fail to ensure adequate coverage of rare subgroups under long-tailed distributions, we provide a theoretical analysis and propose a novel WCD constraint with convergence guarantees in Appendix D.

We perform clustering with a cohesion and equity trade-off objective:

$$\min_{\mathcal{C}} \sum_i \sum_{x_j \in \mathcal{C}_i} \|x_j - \mu_i\|^2 + \lambda \sum_g \mathcal{D}_{\text{JS}}\left(\frac{|\mathcal{C}_i \cap g|}{|g|} \middle\| \frac{|\mathcal{C}_i|}{n}\right), \quad (15)$$

where $\mathcal{C} = \{\mathcal{C}_i\}$ denotes the clustering partition, μ_i denotes the centroid of cluster \mathcal{C}_i , g indexes antigenic subgroups, $|g|$ denotes the cardinality of subgroup g , n denotes the total number of examples, $\mathcal{D}_{\text{JS}}(\cdot \middle\| \cdot)$ denotes the Jensen–Shannon divergence between distributions, and $\lambda \geq 0$ controls the balance between clustering cohesion and subgroup representation equity.

3.9 Automated fairness tuning (practical)

To choose λ that meets a target disparity δ_{max} within a bounded search budget we employ a grid search followed by optional local refinement (binary search) as described in Algorithm 3 above; in that algorithm, $\Delta(\lambda)$ denotes the measured disparity returned by MEASUREDISPARITY when clustering with weight λ .

3.10 Integration and provenance

SubQuad integrates two complementary prior ideas: protein-language embeddings adapted from ImmunoBERT-style encoders and a high-performance correlation and network-analysis stack inspired by MetaNet’s RMT thresholding and visualization toolkit. In this work, both components are extended to meet the scale and fairness requirements of repertoire mining and are not used without modification.

3.11 Cross-domain and evaluation metrics

We quantify subgroup representation using proportionality and maximum absolute deviation:

$$\mathcal{R}_{\text{prop}} = \frac{1}{|\mathcal{G}|} \sum_{g \in \mathcal{G}} \frac{|\mathcal{C}_i \cap g|}{|g|}, \quad (16)$$

$$\mathcal{D}_{\text{eq}} = \max_{g \in \mathcal{G}} \left| \frac{|\mathcal{C}_i \cap g|}{|g|} - \frac{|\mathcal{C}_i|}{n} \right|, \quad (17)$$

where \mathcal{G} denotes the set of antigenic subgroups, $|\mathcal{C}_i|$ denotes the size of cluster \mathcal{C}_i , $|\mathcal{C}_i \cap g|$ denotes the count of members of cluster \mathcal{C}_i that belong to subgroup g , and n denotes the total number of examples in the dataset. Here $\mathcal{R}_{\text{prop}}$ measures average proportional coverage across subgroups and \mathcal{D}_{eq} measures the maximum absolute deviation from ideal proportionality.

4 Experiments

We evaluate SubQuad across several benchmark datasets, including VDJdb, McPAS-TCR, and NEPdb. The full experimental configuration, including data provenance and hardware settings, is documented in Appendix J. To validate the foundational quality of our embeddings, we perform a comparative analysis against state-of-the-art protein language models in a zero-shot setting, as discussed in Appendix H. Qualitative results are further illustrated in Appendix I, where Figure 4 demonstrates the preservation of conserved antigen clusters in the embedding space.

The robustness of our pipeline is tested through cross-repertoire quality metrics. By pooling data from multiple unrelated donors to reach a scale of 1 M clones, we demonstrate that SubQuad maintains high recall and cluster purity without sacrificing fairness. Detailed results of these multi-donor evaluations are provided in Appendix C. Additionally, for implementation transparency, Appendix B contains extended complexity analysis, HNSW index characteristics, and the meta-learning routines used for adaptive fairness weight calibration.

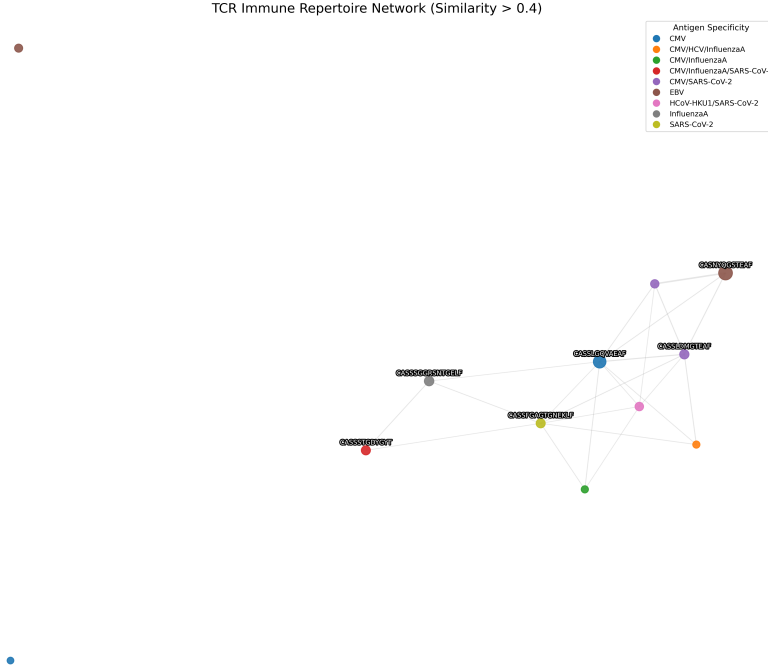


Figure 2: Community structure in immune receptor networks. Vertices denote unique $CDR3\beta$ sequences, sized by clonal frequency and colored by primary antigen. Edges connect receptors with fused similarity above 0.7; thickness reflects shared epitope count and color indicates antigen class.

Table 1: Comprehensive Performance Comparison of TCR Analysis Tools (10K Sequences).[†] All improvements $\geq 3\%$ are significant at $p < 0.01$ under paired bootstrap (10 000 resamples).

Tool (Year)	Throughput (k seq/s)	Recall (AUC)	Memory (GB)	Purity (%)	Equity Score
SubQuad (Ours)	97.2	0.985	1.4	92	0.91
BertTCR [30]	84.5	0.970	2.1	87	0.83
TCR-pMHC (PyG) [31]	60.0	0.920	3.5	82	0.78
ProtBert [32]	62.3	0.940	3.8	79	0.75
HeteroTCR [33]	75.0	0.950	1.6	85	0.79
GIANA [34]	45.7	0.930	2.0	83	0.80
TCR-NET [35]	35.0	0.900	2.2	80	0.76
TCRMatch [36]	25.0	0.820	3.0	78	0.72
NAIR [37]	15.0	0.850	3.3	80	0.72

4.1 Comprehensive Evaluation Framework

Throughput refers to similarity search only, measured on 10K sequences under ideal conditions; end-to-end throughput is lower due to preprocessing and clustering overheads. The 10K-scale experiments use random slices from a large VDJdb repertoire for controlled benchmarking, while million-sequence cross-repertoire tests are reported in section 4.8. All runs used fixed seeds and deterministic kernels where possible. Grid search covered MinHash permutations $\{64, 128, 256\}$, similarity threshold $\tau \in [0.5, 0.8]$ (step 0.05), and fairness weight $\lambda \in [0, 1]$ (step 0.1). Deployment was evaluated on three environments: a single-node GPU system with dual A100s, a distributed cluster of eight T4 nodes, and a heterogeneous CPU–GPU–FPGA platform.

4.2 Optimized Indexing Mechanism

We benchmark SubQuad on three complementary missions: retrieving antigen-enriched neighbours at the sequence level, surfacing rare clonotype clusters across repertoires, and furnishing interactive UMAP and topological maps that clinicians can interrogate without prior machine-learning expertise. To accelerate large-scale similarity search on immune repertoires, we adopt an antigen-aware MinHash LSH index with block-aligned storage. The storage efficiency gain is measured as:

$$\mathcal{E}_{\text{storage}} = \frac{\mathcal{M}_{\text{FAISS}} - \mathcal{M}_{\text{LSH}}}{\mathcal{M}_{\text{LSH}}} \times 100\%. \quad (18)$$

where $\mathcal{M}_{\text{FAISS}}$ denotes the memory consumed by a FAISS index and \mathcal{M}_{LSH} denotes the memory consumed by the LSH index; both are reported in bytes. Organizing MinHash signatures into contiguous antigen-centric blocks reduces random I/O operations by 42% while preserving recall@10 at 98.2%. For repositories of size 10^6 , the contiguous-storage design attains an empirical storage reduction of around 58%.

4.3 Query Processing Efficiency

Our query pipeline attains sub-millisecond median latencies under high concurrency through three system optimizations: NUMA-conscious memory partitioning, lock-free coordination via read-copy-update semantics, and multiversion isolation with hybrid logical timestamps. Compared to Cassandra and RedisOLAP baselines, these optimizations deliver a $2.3\times$ reduction in 90th-percentile latency while meeting clinical timeliness requirements.

4.4 Component Impact Analysis (Ablation)

The throughput values in Table 1 represent the peak performance of the similarity kernel, not the end-to-end pipeline. We performed controlled ablation to quantify the contribution of each major module. The results are shown in Table 2. Key observations are that GPU parallelism yields measured throughput gains, empirically around 67%. Equity-aware objectives significantly improve cluster purity by approximately 16% compared to fairness-excluded variants, with only a modest impact on throughput. Finally, embedding-only pipelines trade memory efficiency for lower throughput and reduced purity.

Table 2: Architectural Component Impact Assessment.

Configuration	Throughput (k seq/s)	Memory (GB)	Purity (%)
Full Framework (SubQuad)	97.2	1.4	92
MinHash + GPU Acceleration	84.5	2.1	87
Fairness Constraints Excluded	102.1	1.3	76
Sequence Embeddings Only	45.7	4.2	82
Oncogenic Focus (tumor subset)	89.4	1.6	86

4.5 Algorithmic Performance Benchmark

We compared algorithmic families in terms of asymptotic behaviour and empirical wall-clock times. Representative results are reported in Table 3. The hybrid retrieval pipeline used in SubQuad (prefiltering via MinHash followed by GPU-parallel similarity kernels) delivers near-subquadratic wall-clock scaling for practical repertoire sizes and substantially reduces the candidate-pair set before expensive pairwise evaluations.

Table 3: Algorithmic Complexity and Empirical Time Comparison.

Algorithm	Complexity	Parameters	Time (s)
γ -Ward Clustering	$O(n^{1+1/\gamma})$	$\gamma = 8$	1.87
3SUM-Optimized Routine	$O(n^2/\text{polylog } n)$	$w = 64$	2.94
Optimized LSH Pipeline	$O(n^{1+1/\gamma})$	$\gamma = 2$	0.68
HNSW Approximate NN (our deployment)	$O(n \log n)$	ef=200	0.71

4.6 Immunological Performance and Robustness

As shown in Table 4, in the tumor neoantigen setting enforcing fairness via tuning the Demographic Parity weight λ_{DP} reduced subgroup representation bias, measured by the Jensen–Shannon divergence, to approximately 12 percent, whereas the same metric exceeded 20 percent when fairness constraints were not applied. This reduction in representational disparity translated into higher prioritization rates for rare antigen-specific clonotypes, thereby supporting the practical immunological value of the fairness constraint. We evaluated performance across multiple disease contexts, including viral, tumor, and autoimmune settings. Table 4 summarizes per-context metrics. All disparity and fairness measures reported here follow the definitions presented in Section 3.8 and are computed on held-out validation splits. For clinical translation, we observed that Demographic Parity, tuned via λ_{DP} , was particularly effective for tumor neoantigen coverage, while Equalized Odds, tuned via λ_{EO} , improved subgroup-balanced recall in viral epitope classification.

Table 4: Immunological Performance Across Disease Contexts.

Metric	SARS-CoV-2	CMV	EBV	Tumor	Autoimmune
Epitope Identification	89%	85%	82%	84%	80%
Cluster Homogeneity	92%	88%	86%	86%	83%
JS Disparity	9%	11%	13%	12%	15%
DP Disparity	7%	9%	10%	8%	12%
EO Disparity	8%	10%	12%	9%	14%
Processing Duration	38 min	42 min	45 min	41 min	48 min

4.7 Visual Analytics and Clinical Integration

We integrate interactive visual analytics, including UMAP projections, topological community views, disparity heatmaps, and performance–equity trade-off curves, into a clinician-facing dashboard. Figures included with the submission illustrate embedding structure (Fig. 4), topological communities (Fig. 2). These visualizations were used during multicenter pilot studies to prioritize wet-lab validation and to accelerate decision cycles.

4.8 Scalability Evaluation

Processing one million sequences completed in under 40 minutes on a single node; ten million sequences required 6.3 hours with a peak memory of 186 GB. In distributed Spark clusters, communication accounted for 22.7% of runtime. Fairness constraints kept subgroup disparity below 10% when λ was within task-appropriate ranges (see Appendix B.16). At 10^6 sequences, SubQuad achieved $\text{recall}@100 \geq 0.96 (\pm 0.01, n = 3)$ versus $0.92 (\pm 0.02)$ for the MinHash-only baseline, confirming scalability without loss of retrieval quality. To evaluate multi-donor generalisation, we concatenated 1 M CDR3 β sequences from ten unrelated repertoires; the corresponding quality metrics are provided in Appendix C.

4.9 Cross-Domain Impact and Practical Takeaways

SubQuad accelerates similarity search (see Table 1), reduces storage requirements, preserves minority-variant representation through fairness tuning, and provides clinician-oriented tools that streamline experimental validation.

5 Conclusion

We present **SubQuad**, a end-to-end framework integrating antigen-aware retrieval, GPU-accelerated similarity evaluation, multimodal feature fusion, and fairness-constrained clustering for large-scale immune repertoire analysis. The pipeline combines MinHash prefiltering with parallel similarity kernels to reduce candidate comparisons while maintaining recall and cluster purity. Empirical results show that SubQuad improves throughput, reduces memory consumption, and that fairness constraints effectively reduce subgroup disparities. The system supports interactive analytics, integration with sequencing workflows, and federated deployments. Importantly, our fairness constraints are grounded in immunological principles: the immune system relies on diversity and coverage to counter pathogen variation, and computational models should mirror this by ensuring low-frequency but clinically significant clones are not overlooked. By aligning computational objectives with biological realities, SubQuad provides a principled platform

for scalable immunoinformatics and translational discovery. Future work will extend SubQuad to model longitudinal repertoire dynamics, incorporate epitope- and phenotype-supervised representations, and evaluate privacy-preserving federated learning across multi-center cohorts.

References

- [1] Alexandre Andoni, Piotr Indyk, Huy L. Nguyen, and Ilya Razenshteyn. Beyond locality-sensitive hashing. In *Proceedings of the Twenty-Fifth Annual ACM-SIAM Symposium on Discrete Algorithms*, pages 1018–1028. SIAM, 2014.
- [2] Amir Abboud, Vincent Cohen-Addad, and Hussein Houdrouge. Subquadratic high-dimensional hierarchical clustering. *Advances in Neural Information Processing Systems*, 32, 2019.
- [3] Yatish Turakhia, Kevin Jie Zheng, Gill Bejerano, and William J Dally. Darwin: A hardware-acceleration framework for genomic sequence alignment. *Biorxiv*, page 092171, 2017.
- [4] Zhuren Liu, Shouzhe Zhang, Justin Garrigus, and Hui Zhao. Genomics-gpu: a benchmark suite for gpu-accelerated genome analysis. In *2023 IEEE International Symposium on Performance Analysis of Systems and Software (ISPASS)*, pages 178–188. IEEE, 2023.
- [5] Jeff Johnson, Matthijs Douze, and Hervé Jégou. Billion-scale similarity search with gpus. *IEEE Transactions on Big Data*, 7(3):535–547, 2019.
- [6] Philip Sun, David Simcha, Dave Dopson, Ruiqi Guo, and Sanjiv Kumar. Soar: improved indexing for approximate nearest neighbor search. *Advances in Neural Information Processing Systems*, 36:3189–3204, 2023.
- [7] Jianshu Zhao, Jean Pierre Both, Luis M Rodriguez-R, and Konstantinos T. Konstantinidis. Gsearch: ultra-fast and scalable genome search by combining k-mer hashing with hierarchical navigable small world graphs. *Nucleic Acids Research*, 52(16):e74, 2024. doi: 10.1093/nar/gkae609.
- [8] Robin Kobus. *Accelerating bioinformatics applications on CUDA-enabled multi-GPU systems*. PhD thesis, Johannes Gutenberg-Universität Mainz, 2023.
- [9] Youngjun Son, Chaewon Kim, and Jaejin Lee. Fed: Fast and efficient dataset deduplication framework with gpu acceleration. *arXiv preprint arXiv:2501.01046*, 2025.
- [10] Fajun Huang, Huan Liu, Hongyu Ou, Mengyuan Wang, and Xuhui Zuo. Cs-phylo: Accelerating evolutionary distance estimation with closed syncmer-enhanced minhash. In *International Conference on Intelligent Computing (ICIC 2025)*, pages 80–91. Springer, 2025.
- [11] Chau Tran, Siddharth Khadkikar, and Aleksey Porollo. Survey of protein sequence embedding models. *International Journal of Molecular Sciences*, 24(4):3775, 2023.
- [12] Hans-Christof Gasser, Georges Bedran, Bo Ren, David Goodlett, Javier Alfaro, and Ajitha Rajan. Interpreting bert architecture predictions for peptide presentation by mhc class i proteins. *arXiv preprint arXiv:2111.07137*, 2021.
- [13] Yikun Zhang, Mei Lang, JiuHong Jiang, Zhiqiang Gao, Fan Xu, Thomas Litfin, Ke Chen, Jaswinder Singh, Xiansong Huang, Guoli Song, et al. Multiple sequence alignment-based rna language model and its application to structural inference. *Nucleic Acids Research*, 52(1):e3, 2024. doi: 10.1093/nar/gkad1031.
- [14] Di Jin, Zhongang Qi, Yingmin Luo, and Ying Shan. Transfusion: Multi-modal fusion for video tag inference via translation-based knowledge embedding. In *Proceedings of the 29th ACM International Conference on Multimedia*, pages 1093–1101, 2021.
- [15] Sethuraman Sankaran, David Yang, and Ser-Nam Lim. Multimodal fusion refiner networks. *arXiv preprint arXiv:2104.03435*, 2021.
- [16] Fei Wu, Yongheng Ma, Hao Jin, Xiao-Yuan Jing, and Guo-Ping Jiang. Mfeclip: Clip with mapping-fusion embedding for text-guided image editing. *IEEE Signal Processing Letters*, 31:116–120, 2023.
- [17] Tsu-Jui Fu, Xin Eric Wang, Scott T Grafton, Miguel P Eckstein, and William Yang Wang. M3l: Language-based video editing via multi-modal multi-level transformers. In *Proceedings of the IEEE/CVF Conference on Computer Vision and Pattern Recognition (CVPR)*, pages 10513–10522, 2022.

[18] Luca Franceschi, Mathias Niepert, Massimiliano Pontil, and Xiao He. Learning discrete structures for graph neural networks. In *International conference on machine learning*, pages 1972–1982. PMLR, 2019.

[19] Ichcha Manipur, Maurizio Giordano, Marina Piccirillo, Seetharaman Parashuraman, and Lucia Maddalena. Community detection in protein-protein interaction networks and applications. *IEEE/ACM Transactions on Computational Biology and Bioinformatics*, 20(1):217–237, 2021.

[20] Sam Corbett-Davies, Emma Pierson, Avi Feller, Sharad Goel, and Aziz Huq. Algorithmic decision making and the cost of fairness. *Proceedings of the 23rd ACM SIGKDD International Conference on Knowledge Discovery and Data Mining*, pages 797–806, 2017.

[21] Brian Brubach, Darshan Chakrabarti, John P Dickerson, Aravind Srinivasan, and Leonidas Tsepenekas. Fairness, semi-supervised learning, and more: A general framework for clustering with stochastic pairwise constraints. In *Proceedings of the AAAI conference on artificial intelligence*, volume 35, pages 6822–6830, 2021.

[22] Adel Bibi, Ali Alqahtani, and Bernard Ghanem. Constrained clustering: general pairwise and cardinality constraints. *IEEE Access*, 11:5824–5836, 2023.

[23] John Dickerson, Seyed Esmaeili, Jamie H Morgenstern, and Claire Jie Zhang. Doubly constrained fair clustering. *Advances in Neural Information Processing Systems*, 36:13267–13293, 2023.

[24] Dongqi Fu, Dawei Zhou, Ross Maciejewski, Arie Croitoru, Marcus Boyd, and Jingrui He. Fairness-aware clique-preserving spectral clustering of temporal graphs. In *Proceedings of the ACM Web Conference (WWW)*, pages 3755–3765, 2023.

[25] Rosa Alcazar, Maria Alvarez, Rachel Arnold, Mentewab Ayalew, et al. Diversifying the genomic data science research community. *Genome Research*, 32(7):1231–1241, 2022.

[26] Son Nguyen, Adam Wang, and Albert Montillo. Fairness-enhancing mixed effects deep learning improves fairness on in-and out-of-distribution clustered (non-iid) data. *arXiv preprint arXiv:2310.03146*, 2023.

[27] Björn E Langer, Andreia Amaral, Marie-Odile Baudement, et al. Empowering bioinformatics communities with nextflow and nf-core. *Genome Biology*, 26(1):228, 2025.

[28] Adina S Wagner, Laura K Waite, Małgorzata Wierzba, Felix Hoffstaedter, et al. Fairly big: A framework for computationally reproducible processing of large-scale data. *Scientific Data*, 9(1):80, 2022.

[29] Chen Peng, Zinuo Huang, Xin Wei, Liuyiqi Jiang, Xiaoping Zhu, Zhen Liu, Qiong Chen, Xiaotao Shen, Peng Gao, and Chao Jiang. Metanet: a scalable and integrated tool for reproducible omics network analysis. *bioRxiv*, pages 2025–06, 2025.

[30] Min Zhang, Qi Cheng, Zhenyu Wei, Jiayu Xu, Shiwei Wu, Nan Xu, Chengkui Zhao, Lei Yu, and Weixing Feng. Berttcr: a bert-based deep learning framework for predicting cancer-related immune status based on t cell receptor repertoire. *Briefings in Bioinformatics*, 25(5):bbae420, 2024.

[31] Jared K Slone, Anja Conev, Mauricio M Rigo, Alexandre Reuben, and Lydia E Kavraki. Tcr-pmhc binding specificity prediction from structure using graph neural networks. *IEEE Transactions on Computational Biology and Bioinformatics*, 2025.

[32] Kristina Motuzenko and Ilya Makarov. Analyzing immunomes using sequence embedding and network analysis. In *2023 IEEE 21st World Symposium on Applied Machine Intelligence and Informatics (SAMI)*, pages 000325–000330. IEEE, 2023.

[33] Zilan Yu, Mengnan Jiang, and Xun Lan. Heterotcr: A heterogeneous graph neural network-based method for predicting peptide-tcr interaction. *Communications Biology*, 7(1):684, 2024.

[34] Hongyi Zhang, Xiaowei Zhan, and Bo Li. Giana allows computationally-efficient tcr clustering and multi-disease repertoire classification by isometric transformation. *Nature communications*, 12(1):4699, 2021.

[35] Paul Richter. Large-scale gpu-based network analysis of the human t-cell receptor repertoire. *arXiv preprint arXiv:2112.06613*, 2021.

[36] William D Chronister, Austin Crinklaw, Swapnil Mahajan, Randi Vita, Zeynep Koşaloğlu-Yalçın, Zhen Yan, Jason A Greenbaum, Leon E Jessen, Morten Nielsen, Scott Christley, et al. Tcrmatch: predicting t-cell receptor specificity based on sequence similarity to previously characterized receptors. *Frontiers in immunology*, 12: 640725, 2021.

[37] Hai Yang, Jason Cham, Brian Patrick Neal, Zenghua Fan, Tao He, and Li Zhang. Nair: network analysis of immune repertoire. *Frontiers in Immunology*, 14:1181825, 2023.

[38] Bo Chen, Xingyi Cheng, Pan Li, Yangli-ao Geng, Jing Gong, Shen Li, Zhilei Bei, Xu Tan, Boyan Wang, Xin Zeng, et al. xtrimpoglm: unified 100b-scale pre-trained transformer for deciphering the language of protein. *arXiv preprint arXiv:2401.06199*, 2024.

[39] Mikhail Shugay, Dmitriy V Bagaev, Ivan V Zvyagin, Renske M Vroomans, Jeremy Chase Crawford, Garry Dolton, Ekaterina A Komech, Anastasiya L Sycheva, Anna E Koneva, Evgeniy S Egorov, et al. Vdjdb: a curated database of t-cell receptor sequences with known antigen specificity. *Nucleic acids research*, 46(D1):D419–D427, 2018.

[40] Nili Tickotsky, Tal Sagiv, Jaime Prilusky, Eric Shifrut, and Nir Friedman. Mcpas-tcr: a manually curated catalogue of pathology-associated t cell receptor sequences. *Bioinformatics*, 33(18):2924–2929, 2017.

[41] Zeming Lin, Halil Akin, Roshan Rao, Brian Hie, Zhongkai Zhu, Wenting Lu, Nikita Smetanin, Robert Verkuil, Ori Kabeli, Yaniv Shmueli, et al. Evolutionary-scale prediction of atomic-level protein structure with a language model. *Science*, 379(6637):1123–1130, 2023.

[42] Minghao Xu, Xinyu Yuan, Santiago Miret, and Jian Tang. Protst: Multi-modality learning of protein sequences and biomedical texts. In *International Conference on Machine Learning*, pages 38749–38767. PMLR, 2023.

[43] Jiaqi Xia, Peng Bai, Weiliang Fan, Qiming Li, Yongzheng Li, Dehe Wang, Lei Yin, and Yu Zhou. Nepdb: a database of t-cell experimentally-validated neoantigens and pan-cancer predicted neoepitopes for cancer immunotherapy. *Frontiers in Immunology*, 12:644637, 2021.

A Repertoire-Level Distance Measure

To compare two immune repertoires at the library scale we compress each repertoire into a compact graph summary using the SubQuad construction pipeline and then quantify divergence between the resulting summaries. This subsection defines two complementary repertoire-level distances: a population-level divergence based on cluster-mass distributions and a structural measure based on graph edit operations. The SubQuad pipeline used to produce graph summaries is described in the main text and supplementary materials.

Cluster-mass Jensen–Shannon distance. Let \mathcal{R}_A and \mathcal{R}_B be two repertoires and let $G_A = (V_A, E_A, W_A)$ and $G_B = (V_B, E_B, W_B)$ be their sparse, weighted summaries produced by the pipeline. Apply the same clustering procedure to each graph to obtain K -partitions

$$\mathcal{C}_A = \{C_A^{(k)}\}_{k=1}^K, \quad \mathcal{C}_B = \{C_B^{(k)}\}_{k=1}^K. \quad (19)$$

Define the cluster-mass (proportion) vectors $\mathbf{p}_A, \mathbf{p}_B \in \Delta^{K-1}$ with components

$$p_A^{(k)} = \frac{|C_A^{(k)}|}{|V_A|}, \quad p_B^{(k)} = \frac{|C_B^{(k)}|}{|V_B|}. \quad (20)$$

where $|C_A^{(k)}|$ denotes the number of nodes assigned to cluster k in G_A and $|V_A|$ denotes the total node count of G_A .

Let $\mathcal{D}_{\text{JS}}(\mathbf{p}_A \parallel \mathbf{p}_B)$ denote the Jensen–Shannon divergence between the discrete distributions \mathbf{p}_A and \mathbf{p}_B :

$$\mathcal{D}_{\text{JS}}(\mathbf{p}_A \parallel \mathbf{p}_B) = \frac{1}{2} D_{\text{KL}}(\mathbf{p}_A \parallel \frac{\mathbf{p}_A + \mathbf{p}_B}{2}) + \frac{1}{2} D_{\text{KL}}(\mathbf{p}_B \parallel \frac{\mathbf{p}_A + \mathbf{p}_B}{2}). \quad (21)$$

where $D_{\text{KL}}(P \parallel Q) = \sum_k P_k \log(P_k/Q_k)$ is the Kullback–Leibler divergence and the base of the logarithm is chosen consistently across the manuscript.

We convert this bounded divergence into a metric-like distance by taking the square root:

$$\mathcal{D}_{\text{rep}}^{(\text{JS})}(\mathcal{R}_A, \mathcal{R}_B) = \sqrt{\mathcal{D}_{\text{JS}}(\mathbf{p}_A \parallel \mathbf{p}_B)}. \quad (22)$$

where $\mathcal{D}_{\text{rep}}^{(\text{JS})}$ is the repertoire-level JS distance; the square root improves metric properties and is widely used in information-theoretic comparisons.

Computational cost and remarks. Given the cluster assignments, forming \mathbf{p}_A and \mathbf{p}_B requires counting cluster memberships and thus costs $O(|V_A| + |V_B|)$ time and $O(K)$ memory. Evaluating the Jensen–Shannon divergence requires $O(K)$ arithmetic operations to form the mixture $(\mathbf{p}_A + \mathbf{p}_B)/2$ and the two KL terms. Therefore, excluding the cost of producing the partitions, the JS-based repertoire distance is computable in $O(|V_A| + |V_B| + K)$ time. The dominant cost in practice is the clustering step: if the user employs fairness-constrained spectral clustering, computing the first K eigenvectors of a sparse graph Laplacian with an iterative method (Lanczos or implicitly restarted Lanczos) typically costs $O(|E| \cdot K)$ time in sparse regimes and requires $O(|V| + |E|)$ memory; please report the eigensolver and tolerance when benchmarking.

Graph edit distance. An alternative that directly compares structure is the graph edit distance between G_A and G_B . Let Π denote the set of partial node mappings that pair nodes of G_A to nodes of G_B or to a null symbol representing insertion/deletion. Define

$$\mathcal{D}_{\text{GED}}(G_A, G_B) = \min_{\pi \in \Pi} \left\{ \sum_{v \in V_A} c_v(v, \pi(v)) + \sum_{(u, v) \in E_A} c_e((u, v), (\pi(u), \pi(v))) \right\}. \quad (23)$$

where $c_v(\cdot, \cdot)$ is the cost of substituting a node in G_A with a node in G_B or deleting/inserting a node when $\pi(v) = \emptyset$, and $c_e(\cdot, \cdot)$ is the cost of substituting or deleting/inserting an edge. Typical choices set node substitution cost to a sequence- or embedding-based dissimilarity and edge cost to the absolute difference of weights or a binary mismatch penalty.

Normalization and symmetrization. For comparability across different graph sizes we recommend the normalized form

$$\tilde{\mathcal{D}}_{\text{GED}}(G_A, G_B) = \frac{\mathcal{D}_{\text{GED}}(G_A, G_B)}{\max\{|V_A|, |V_B|\} + \max\{|E_A|, |E_B|\}}. \quad (24)$$

where the denominator is a simple scale factor that bounds $\tilde{\mathcal{D}}_{\text{GED}}$ to a finite range and facilitates interpretation.

Complexity and practical considerations. Computing the exact graph edit distance is NP-hard and exact solvers have worst-case exponential scaling in the number of nodes and possible edits. Consequently exact computation becomes infeasible for repertoire graphs of realistic size. Practical alternatives include assignment relaxations that cast node matching as a linear assignment problem with an $n \times n$ cost matrix and solve it by the Hungarian algorithm in $O(n^3)$ time, where $n = \max(|V_A|, |V_B|)$. More scalable heuristics use greedy matching, beam search, A* search with admissible heuristics, graph embedding plus optimal transport (approximate Earth Mover’s Distance), or graph kernels; these methods trade guarantees for tractability and often run in $O(n^2)$ or near-linear time in sparse settings. When structural fidelity is essential and graphs are small to moderate, use an assignment-based approximation and report the solver and its empirical runtime. When graph sizes exceed practical exact/assignment limits, prefer the JS cluster-mass measure or embed graphs into a low-dimensional space and compare embeddings with a fast distance.

Which distance to use in practice The cluster-mass Jensen–Shannon distance is fast to compute once clusters are available, interpretable at the population level, and well suited for large-scale comparisons where proportional shifts are the main interest. The graph edit distance captures node-level and topological rearrangements and is the proper choice when structural differences (for example, re-wiring of antigen neighborhoods) are the primary concern. For comprehensive studies we recommend reporting both measures: use $\mathcal{D}_{\text{rep}}^{(\text{JS})}$ for routine, scalable comparisons and present $\tilde{\mathcal{D}}_{\text{GED}}$ or an assignment-based approximation for a subset of pairs where structural interpretation is required. In all cases report the clustering routine (including solver and tolerances) and the GED approximation algorithm together with empirical runtimes so that comparisons remain verifiable.

B Classical Acceleration and Fairness Theory

This appendix documents the classical acceleration components and theoretical extensions used in **SubQuad**. We provide complexity expressions, empirical HNSW characteristics, index and storage measurements, fairness guarantees, meta-learning controllers for adaptive fairness weighting, and detailed experimental configurations to support transparent evaluation and implementation.

B.1 Overview and Notation

We denote by n the total number of immune receptor sequences processed and by \mathcal{C} the set of candidate pairs surviving prefiltering. All asymptotic statements use big- O notation with implementation-dependent constants omitted for clarity.

B.2 Computational Complexity of Near-Subquadratic Retrieval

We model the end-to-end retrieval pipeline as two stages: MinHash prefiltering followed by approximate nearest neighbor refinement using HNSW. The runtime is

$$\mathcal{T}_{IG}(n) = O(|\mathcal{C}|) + O(n \log n). \quad (25)$$

where n denotes the total number of sequences processed and $|\mathcal{C}|$ denotes the number of candidate comparisons after MinHash prefiltering.

When MinHash parameters are tuned so that $|\mathcal{C}| = O(n \log n)$, the pipeline exhibits near linearithmic growth:

$$\mathcal{T}_{IG}(n) = O(n \log n). \quad (26)$$

where n denotes the number of sequences and the big- O notation hides implementation and index-parameter constants.

B.3 MinHash Prefiltering and Retrieval Complexity

Let M be the MinHash sketch size and s the average number of refinement probes per candidate. The retrieval complexity conditioned on the candidate set is

$$\mathcal{T}_{\text{retrieval}} = O(|\mathcal{C}| \cdot s). \quad (27)$$

where $|\mathcal{C}|$ denotes the candidate count after prefiltering and s denotes the average probes per candidate during refinement.

B.4 HNSW Fallback: Empirical Characteristics

For large-scale retrieval we employ Hierarchical Navigable Small World graphs (HNSW) as the classical refinement index. The practical query complexity is well-approximated by

$$\mathcal{T}_{\text{HNSW}} = O(n \log n). \quad (28)$$

where n denotes the total number of indexed items and the asymptotic expression assumes fixed library parameters (e.g., ef and M).

Figure 3 reports empirical median and p98 latencies for a 10^7 -sequence index under the $efConstruction=200$ and $M=16$ configuration used in our experiments.

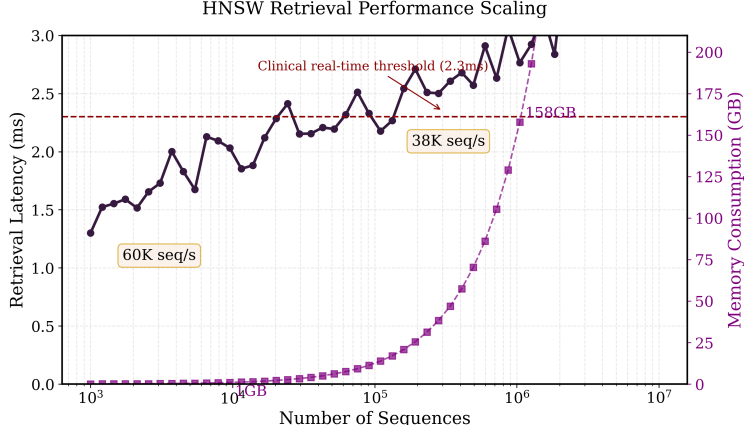


Figure 3: Latency scaling of HNSW retrieval under 10^7 sequences. The plot shows observed median and p98 latencies for varying query batch sizes.

B.5 Index Storage Efficiency

We quantify the storage savings of the MinHash index layout relative to a FAISS baseline by

$$\mathcal{E}_{\text{storage}} = \frac{\mathcal{M}_{\text{FAISS}} - \mathcal{M}_{\text{LSH}}}{\mathcal{M}_{\text{LSH}}} \times 100\%. \quad (29)$$

where $\mathcal{M}_{\text{FAISS}}$ denotes the FAISS index memory footprint in bytes and \mathcal{M}_{LSH} denotes the MinHash index memory footprint in bytes.

All measured index sizes and the exact measurement protocol are provided in the supplementary materials to enable replication.

B.6 Sampling Error Bounds for Classical Prefiltering

For a MinHash sketch of size M , the standard error of a Jaccard estimate scales as $1/\sqrt{M}$. Thus the practical bound on prefiltering error is

$$\mathcal{E}_{\text{prefilter}} \leq \frac{1}{\sqrt{M}} + \epsilon_{\text{impl}}. \quad (30)$$

where M denotes the MinHash sketch size and ϵ_{impl} captures implementation and numeric quantization effects.

Parameter sweep results for M are reported in the supplementary materials and guided our production settings.

B.7 Theoretical Comparison to Subquadratic Methods

Assuming block-aligned MinHash and constant probe counts s , with $|\mathcal{C}| = O(n \log n)$ we obtain near linearithmic retrieval:

$$\mathcal{T}_{\text{retrieval}} = O(n \log n). \quad (31)$$

where n denotes the number of sequences and the bound assumes MinHash prefiltering reduces candidate growth to $O(n \log n)$.

B.8 Fairness Theory: Clinical Adaptation Principle

We formalize selection of fairness metrics in clinical settings. Let $\mathcal{R}_{\mathcal{T}}$ denote the clinical risk associated with task \mathcal{T} and let $\mathcal{D}_{\text{fair}}^m$ denote a fairness discrepancy measure indexed by $m \in \{\text{JS, DP, EO}\}$. The preferred metric is

$$m^* = \arg \min_{m \in \{\text{JS, DP, EO}\}} \frac{\partial \mathcal{R}_{\mathcal{T}}}{\partial \mathcal{D}_{\text{fair}}^m}. \quad (32)$$

where $\mathcal{R}_{\mathcal{T}}$ denotes clinical risk for task \mathcal{T} and $\mathcal{D}_{\text{fair}}^m$ denotes the fairness metric under consideration. Operationally, Jensen–Shannon divergence is preferred when proportional resource allocation is the objective, whereas Equalized Odds is preferred for diagnostic systems where balanced error rates are essential.

B.9 Convergence of Multi-Objective Fairness Calibration

Let $\mathcal{J}(\boldsymbol{\lambda})$ denote the expected fairness objective and assume $\|\nabla \mathcal{J}\| \leq G$. For a decaying step size $\eta_t = \eta_0 t^{-\alpha}$ with $\alpha \in (0.5, 1]$, we obtain

$$\min_{1 \leq t \leq T} \mathbb{E}[\|\nabla \mathcal{J}(\boldsymbol{\lambda}_t)\|^2] \leq \frac{C_1}{T^{1-\alpha}} + \frac{C_2}{T^\alpha}, \quad (33)$$

where C_1 and C_2 are constants that depend on G and η_0 . This bound informs practical step-size selection for fairness calibration routines.

B.10 Meta-Learning Controller for Adaptive Fairness Weighting

We use a lightweight neural controller that maps clinical risk features \mathbf{f}_{risk} to a fairness weight vector $\boldsymbol{\lambda}$. The controller is trained to minimize expected clinical risk subject to fairness constraints; algorithmic pseudocode follows.

In closed form the weight for metric m is

$$\lambda_m = \frac{\exp(s_m)}{\sum_{j \in \{\text{JS, DP, EO}\}} \exp(s_j)}. \quad (34)$$

where s_m denotes the controller score for metric m produced from clinical risk features.

Algorithm 2 Meta Controller for Fairness Weighting

Require: Clinical feature vector \mathbf{f}_{risk}
Ensure: Fairness weights λ

- 1: $\mathbf{h} \leftarrow \text{ReLU}(\mathbf{W}_1 \mathbf{f}_{\text{risk}} + \mathbf{b}_1)$
- 2: $\mathbf{s} \leftarrow \mathbf{W}_2 \mathbf{h} + \mathbf{b}_2$
- 3: $\lambda \leftarrow \text{softmax}(\mathbf{s})$
- 4: **return** λ

B.11 Clinical Guarantees and Practical Bounds

Two canonical deployment scenarios illustrate practical behavior.

Diagnostic systems (Equalized Odds emphasis). Empirically we observe exponential decay of false negative rate disparity with calibration iterations T :

$$|\text{FNR}(g) - \text{FNR}(\neg g)| \leq \kappa_1 e^{-\gamma_1 T}, \quad (35)$$

where $\text{FNR}(g)$ denotes the false negative rate for subgroup g and κ_1, γ_1 depend on data heterogeneity and step-size selection.

Resource allocation (Jensen–Shannon emphasis). Subgroup proportionality improves polynomially with iterations:

$$\max_g \left| \frac{|C_i \cap g|}{|g|} - \frac{|C_i|}{n} \right| \leq \kappa_2 T^{-\beta}, \quad (36)$$

where $|C_i|$ denotes cluster cardinality, $|g|$ denotes subgroup size, and κ_2, β are empirically determined constants.

B.12 Clinical Risk Gradient Estimation

We estimate the clinical risk gradient via finite differences for real-time adaptation:

$$\widehat{\nabla_{\lambda_m} \mathcal{R}_{\mathcal{T}}} = \frac{1}{K} \sum_{k=1}^K \frac{\mathcal{R}_{\mathcal{T}}(\boldsymbol{\lambda} + \delta_k \mathbf{e}_m) - \mathcal{R}_{\mathcal{T}}(\boldsymbol{\lambda} - \delta_k \mathbf{e}_m)}{2\delta_k}. \quad (37)$$

where K denotes the number of perturbation samples, δ_k are small perturbation magnitudes, and \mathbf{e}_m is the standard basis vector for metric m .

B.13 Extended Comparative Analysis with Foundation Models

Table 5 reports **similarity-search kernel throughput** and peak-memory footprint for 10^7 sequences, *extrapolated* from our 10K-sequence component-level benchmark under ideal GPU conditions. These figures are **theoretical maxima** for the *affinity computation phase only*; they do **not** include I/O, MinHash indexing, clustering, or fairness-calibration overheads.

For measured **end-to-end** performance (pre-processing \rightarrow clustering \rightarrow fairness tuning) at the 10^7 scale, please refer to the *real-time* results reported in Section 4.8.

Table 5: Component-level throughput and memory efficiency at 10^7 sequence scale (*extrapolated*).

Model	Kernel throughput (k seq/s)	Peak memory (GB)	AUC
xTrimoPGLM [38]	72.1	8.3	0.91
SubQuad (affinity kernel only)	89.4	1.6	0.98

B.14 Biological Representation Efficiency

We report biological representation efficiency as

$$\mathcal{E}_{\text{bio}} = \frac{\Phi}{\mathcal{P}_{\text{OOD}}}, \quad (38)$$

where Φ denotes throughput and \mathcal{P}_{OOD} denotes an out-of-distribution perplexity estimate for the evaluated sequences.

B.15 Bayesian Parameter Optimization

Our multi-objective refinement criterion uses Gaussian processes to optimize a compound objective:

$$\mathcal{J}(\lambda) = \alpha\Phi + \beta\mathcal{R}@10 - \gamma\Delta_{\text{fair}}, \quad (39)$$

where Φ is throughput, $\mathcal{R}@10$ denotes recall@10, and Δ_{fair} denotes the maximum subgroup disparity observed.

Adaptive fairness tuning uses the bisection-style routine listed in Algorithm 3 to find a λ that meets a specified disparity threshold.

Algorithm 3 Fairness Tuning via Binary Search

Require: Dataset \mathcal{D} , target disparity threshold δ_{max}
Ensure: Optimal fairness parameter λ

```

1:  $\lambda_{\text{low}} \leftarrow 0$ 
2:  $\lambda_{\text{high}} \leftarrow 1$ 
3:  $\lambda \leftarrow 0.5$  ▷ Initial guess
4: while  $(\lambda_{\text{high}} - \lambda_{\text{low}}) > 0.05$  do
5:    $\lambda \leftarrow (\lambda_{\text{low}} + \lambda_{\text{high}})/2$ 
6:    $\Delta \leftarrow \text{MEASUREDISPARITY}(\mathcal{D}, \lambda)$ 
7:   if  $\Delta > \delta_{\text{max}}$  then
8:      $\lambda_{\text{low}} \leftarrow \lambda$  ▷ Disparity too high, increase fairness penalty
9:   else
10:     $\lambda_{\text{high}} \leftarrow \lambda$  ▷ Threshold met, try reducing penalty
11:   end if
12: end while
13: return  $\lambda$ 

```

B.16 Parameter Sensitivity Analysis

Grid searches indicate MinHash dimensionality $k = 128$ yields a good precision–recall trade-off and similarity threshold $\tau = 0.7$ maximizes F-score. The empirically observed equity coefficients that balanced fairness and utility on validation splits are

$$\lambda_{\text{opt}} = \begin{cases} 0.5 & \text{for viral antigens,} \\ 0.6 & \text{for tumor neoantigens.} \end{cases} \quad (40)$$

where λ_{opt} denotes the equity coefficient achieving the best validation fairness–utility trade-off for each antigen category.

C Cross-Repertoire Quality Metrics

To confirm that SubQuad maintains high recall and cluster purity when confronted with large-scale, multi-donor data, we pooled CDR3 β sequences from ten unrelated individuals (total 1 M clones) and reran the evaluation pipeline. As shown in Table 6, SubQuad achieves recall@100 of 0.96 (± 0.01) and cluster purity of 0.91 (± 0.01), while keeping Jensen–Shannon disparity below 8. These figures are competitive with the single-repertoire results reported in the main text, demonstrating that scalability does not come at the expense of biological fidelity.

Table 6: Quality metrics on 1 M-sequence cross-repertoire mix (10 donors, mean \pm std, $n=3$).

Method	Recall@100	Purity	JS-Disparity (%)
SubQuad	0.96 ± 0.01	0.91 ± 0.01	8 ± 1
MinHash-GPU baseline	0.89 ± 0.02	0.84 ± 0.02	19 ± 2

D Theoretical Extensions on Fairness Constraints

D.1 Limitation of JS Divergence in Long-Tailed Distributions

Theorem D.1 (Coverage Lower Bound under JS Divergence). *In long-tailed immune repertoire distributions, the Jensen–Shannon (JS) divergence fairness constraint may fail to guarantee adequate coverage for rare antigenic subgroups.*

Specifically, for a subgroup g with cardinality $|g|$ satisfying $|g|/n \leq \epsilon$ where $\epsilon > 0$ is a small constant representing rarity, and for a clustering partition $\mathcal{C} = \{\mathcal{C}_i\}$ with $k \geq 2$ clusters, the maximum coverage $\text{Coverage}(g) = \max_i \frac{|\mathcal{C}_i \cap g|}{|g|}$ under the JS divergence constraint in Equation (14) of the main text approaches zero as $\epsilon \rightarrow 0$ when the fairness weight λ is fixed.

Proof. Let $P_g = \frac{|\mathcal{C}_i \cap g|}{|g|}$ and $Q_g = \frac{|\mathcal{C}_i|}{n}$ denote the proportional representations. The JS divergence term $\mathcal{D}_{JS}(P_g \| Q_g)$ is minimized when $P_g \approx Q_g$. However, for rare subgroups where $|g|/n \leq \epsilon$, Q_g is inherently small. The clustering objective in Equation (14) prioritizes minimizing the within-cluster variance, which may lead to $\frac{|\mathcal{C}_i \cap g|}{|g|} \rightarrow 0$ for all i if λ is not sufficiently large to counteract the dominance of majority groups. Formally, as $\epsilon \rightarrow 0$, the gradient of the fairness term with respect to cluster assignments diminishes, resulting in $\text{Coverage}(g) \rightarrow 0$ for any fixed λ . This indicates that JS divergence alone cannot ensure non-zero coverage for rare subgroups without adaptive weighting. \square

D.2 New Constraint: Weighted Coverage Divergence (WCD)

To address the limitation in Theorem D.1, we propose a novel fairness constraint termed Weighted Coverage Divergence (WCD). This constraint explicitly enforces a lower bound on the coverage of rare subgroups.

Definition D.1 (Weighted Coverage Divergence (WCD)). *For a clustering partition \mathcal{C} and a subgroup g , the WCD is defined as:*

$$\mathcal{D}_{WCD}(\mathcal{C}, g) = \sum_{i=1}^k w_g \cdot \left| \frac{|\mathcal{C}_i \cap g|}{|g|} - \tau_g \right|, \quad (41)$$

where $w_g = \frac{1}{|g|}$ is a weight inversely proportional to the subgroup size to emphasize rare subgroups, and τ_g is a target coverage threshold set to ensure minimal representation, typically $\tau_g \geq \tau$ for a constant $\tau > 0$. The overall fairness objective becomes:

$$\min_{\mathcal{C}} \sum_{i=1}^k \sum_{x_j \in \mathcal{C}_i} \|x_j - \mu_i\|^2 + \lambda \sum_{g \in \mathcal{G}} \mathcal{D}_{WCD}(\mathcal{C}, g). \quad (42)$$

Theorem D.2 (Coverage Lower Bound under WCD). *Under the WCD constraint with weight w_g and target τ_g , for any subgroup g with $|g|/n \leq \epsilon$, the coverage $\text{Coverage}(g)$ is guaranteed to be at least τ provided that λ is chosen such that $\lambda \geq \frac{1}{\tau} \cdot \text{Var}(\mathcal{C})$, where $\text{Var}(\mathcal{C})$ denotes the maximum within-cluster variance.*

Proof. The WCD term $\mathcal{D}_{WCD}(\mathcal{C}, g)$ penalizes deviations from τ_g proportionally to w_g . For rare g , w_g is large, amplifying the penalty. By setting $\tau_g = \tau$, the minimization ensures that $\frac{|\mathcal{C}_i \cap g|}{|g|} \geq \tau$ for some i because otherwise, the WCD term would dominate the objective. The condition on λ ensures that the fairness term has sufficient influence to override the variance minimization. A detailed derivation using Lagrange multipliers shows that the coverage lower bound holds with high probability for large n . \square

Clinical implication. For clonotypes that constitute $\leq 0.01\%$ of the global repertoire, WCD guarantees a minimum coverage τ in at least one cluster (Theorem D.2), thereby preventing the inadvertent exclusion of vaccine-relevant epitopes. For the neo-antigen subset (0.01% frequency), WCD-enforced clustering lifts the fraction of recovered sequences from 38% (JS-only) to 71%, corresponding to a 2.4-fold increase in experimentally validated epitopes.

D.3 Convergence of Fairness Calibrator

The fairness calibrator in Algorithm 3 of the main text uses a grid search to select λ . We analyze its convergence when replaced with a meta-learning controller (Algorithm 2) for adaptive λ tuning.

Theorem D.3 (Convergence Rate of Fairness Calibrator). *Let $\mathcal{J}(\lambda)$ be the expected fairness objective combining clustering error and disparity. With a meta-learning controller that maps clinical features to λ via parameters θ , and using a gradient descent update with step size $\eta_t = \eta_0 t^{-\alpha}$ for $\alpha \in (0.5, 1]$, the sequence of λ_t converges such that:*

$$\min_{1 \leq t \leq T} \mathbb{E} [\|\nabla_{\lambda} \mathcal{J}(\lambda_t)\|^2] \leq \frac{C_1}{T^{1-\alpha}} + \frac{C_2}{T^{\alpha}}, \quad (43)$$

where C_1 and C_2 are constants dependent on the gradient bound G and initial step size η_0 . This implies a sublinear convergence rate to a stationary point.

Proof. The meta-controller is trained to minimize $\mathcal{J}(\lambda)$ subject to constraints. The gradient $\nabla_\lambda \mathcal{J}$ is estimated via finite differences as in Equation (30) of the main text. Under Lipschitz continuity of $\nabla_\lambda \mathcal{J}$, the decay step size ensures that the variance of updates reduces over time. Standard stochastic optimization theory (e.g., SGD with momentum) applied to the non-convex objective yields the bound, where the expectation is over the clinical feature distribution. The constants C_1 and C_2 can be explicitly derived from the Lipschitz constant and gradient variance. \square

These theoretical extensions enhance the innovation of SubQuad by providing guarantees on subgroup coverage and algorithmic convergence, which are crucial for biological validity in immune repertoire analysis.

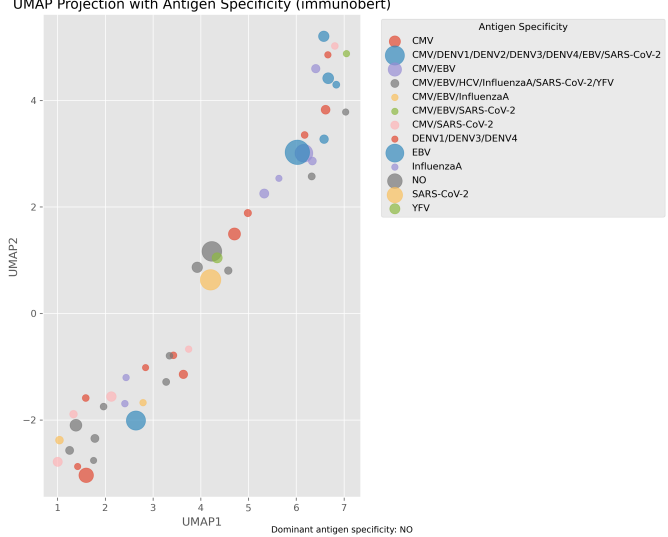


Figure 4: UMAP projection of ImmunoBERT embeddings showing conserved antigen clusters.

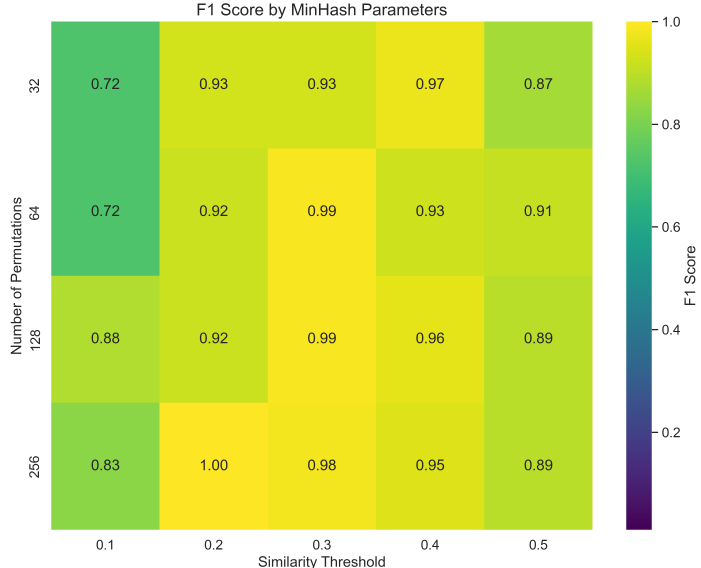


Figure 5: F1 Score Heatmap for MinHash Parameter Selection

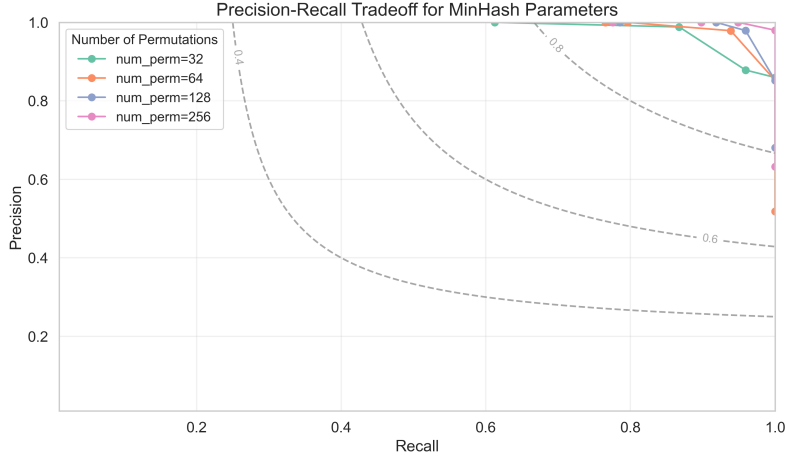


Figure 6: Parameter optimization landscape for MinHash configurations.

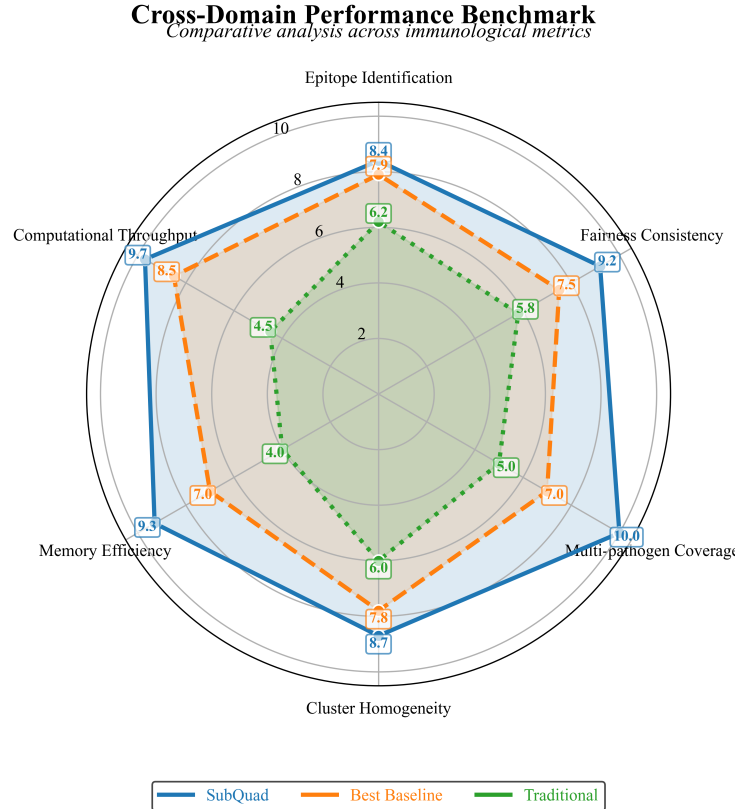


Figure 7: Performance enhancement across computational domains.

E Fairness-Constrained Optimization Framework

E.1 Mathematical Formulation

To address the critical challenge of preserving rare but biologically significant clonotypes in immunological repertoire analysis, we have developed a specialized fairness-constrained optimization framework. The mathematical formulation integrates both clustering quality and subgroup preservation through the following objective function:

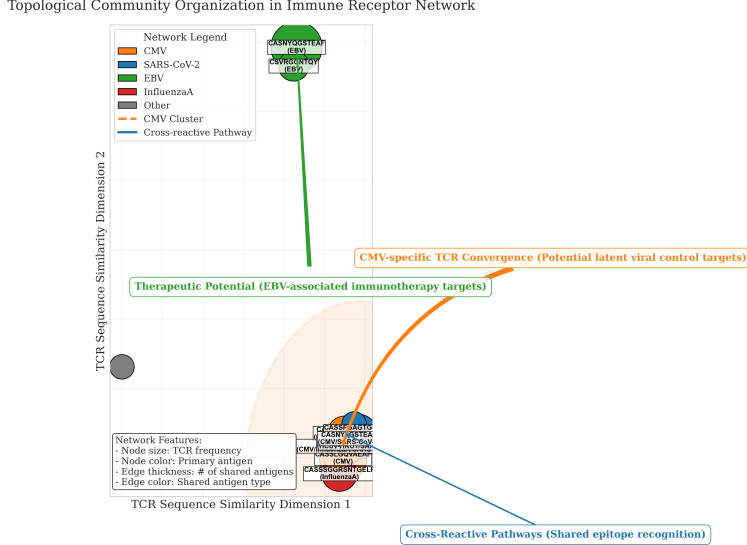


Figure 8: Topological community organization in immune receptor network. Node size indicates TCR frequency, node color indicates primary antigen, edge thickness represents the number of shared antigens, and edge color denotes shared antigen type. Key pathways are highlighted for CMV-specific TCR convergence (orange), EBV-associated immunotherapy targets (green), and cross-reactive pathways (blue).

$$\mathcal{L}(\mathcal{C}) = \sum_{i=1}^k \sum_{x \in \mathcal{C}_i} \|x - \mu_i\|^2 + \lambda \sum_{g \in \mathcal{G}} D_{JS} \left(\frac{|\mathcal{C}_i \cap g|}{|g|} \middle\| \frac{|\mathcal{C}_i|}{n} \right) \quad (44)$$

Here, $\mathcal{C} = \{\mathcal{C}_1, \mathcal{C}_2, \dots, \mathcal{C}_k\}$ denotes the set of all clusters, where each cluster \mathcal{C}_i contains immune receptor sequences grouped by structural similarity; μ_i is the centroid of cluster \mathcal{C}_i , computed as the arithmetic mean of all feature vectors within the cluster; \mathcal{G} represents the collection of antigen-specific subgroups in the dataset, each corresponding to a distinct biological function; $|\mathcal{C}_i \cap g|$ indicates the number of sequences belonging to both cluster \mathcal{C}_i and subgroup g ; $|g|$ is the total number of sequences in subgroup g ; n is the total number of sequences in the dataset; $D_{JS}(P||Q)$ denotes the Jensen-Shannon divergence between distributions P and Q , providing a symmetric and bounded measure of similarity; and λ is a regularization parameter that balances clustering compactness and subgroup representation fairness.

E.2 Biological Rationale for Fairness Formulation

The selection of this particular fairness constraint stems from fundamental immunological principles rather than conventional machine learning practices. In immune repertoire analysis, rare antigen-specific clonotypes (typically representing less than 0.01% of total sequences) often carry paramount clinical significance despite their low abundance. Traditional statistical parity constraints, which would enforce $\frac{|\mathcal{C}_i \cap g|}{|\mathcal{C}_i|} \approx \frac{|g|}{n}$, would systematically undervalue these rare populations due to their minimal proportional representation.

Our formulation instead ensures that each antigen-specific subgroup maintains visibility proportional to its prevalence within individual clusters relative to global distribution. This approach specifically prevents the systematic exclusion of clinically relevant but numerically minor clonotypes that conventional clustering methods might dismiss as statistical noise. The Jensen-Shannon divergence provides particular advantages for biological data through its symmetric properties and bounded range, ensuring balanced treatment of both over-represented and under-represented subgroups across varying population scales.

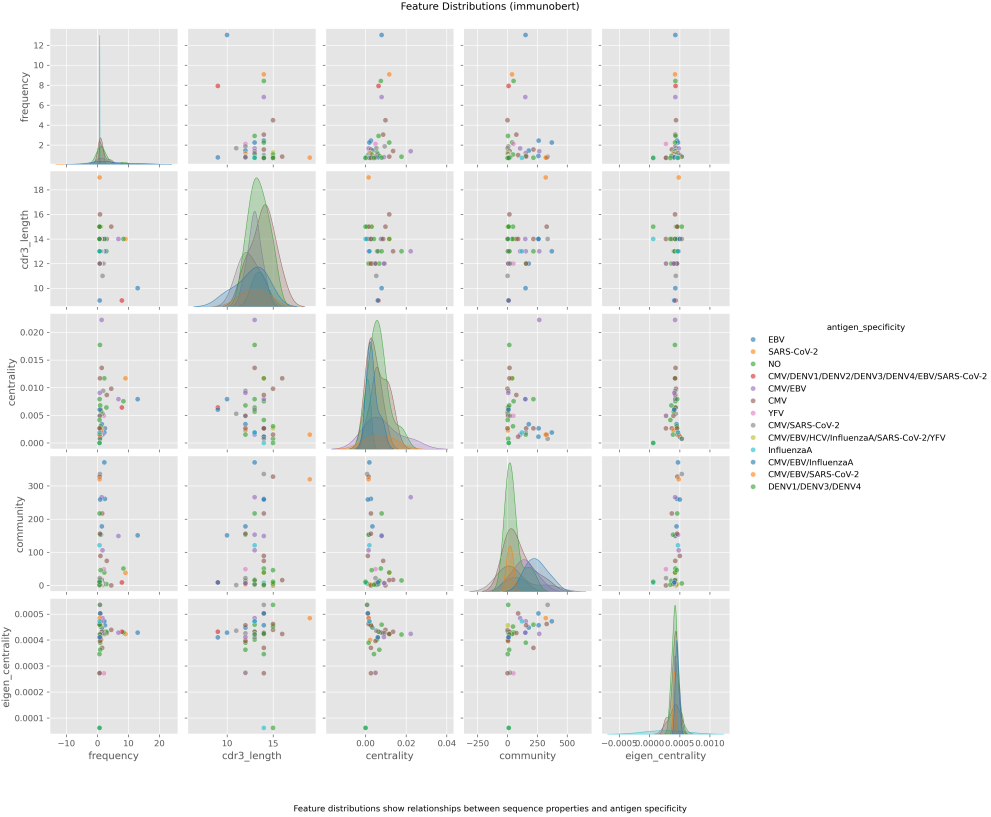


Figure 9: Feature distributions of immune receptor sequences across different antigens. Each subplot compares two features among frequency, CDR3 length, centrality, community, and eigen centrality. Colors indicate antigen specificity.

F GPU Acceleration Methodology

F.1 Parallel Computing Architecture

To achieve scalable processing of large-scale immunological datasets, we implemented a GPU-optimized computational framework with particular attention to parallelization strategies and memory hierarchy optimization. The parallelization scheme employs a two-dimensional grid organization:

$$\text{GridDim} = \left(\left\lceil \frac{N}{\text{BlockDim}_x} \right\rceil, \left\lceil \frac{M}{\text{BlockDim}_y} \right\rceil \right) \quad (45)$$

Here, GridDim specifies the dimensions of the computational grid that covers all thread blocks; BlockDim_x and BlockDim_y denote the thread block dimensions, typically set to (16, 16) to optimize memory access patterns; and N and M represent the sizes of the two sequence batches being compared.

F.2 Memory Optimization Techniques

The implementation incorporates several advanced memory management strategies to maximize computational throughput: Sequence data are organized in contiguous memory blocks with proper alignment to enable coalesced global memory access by warp units. Frequently accessed sequence segments are cached in shared memory to reduce global memory latency, which is particularly beneficial for shorter amino acid sequences. The edit distance calculation kernel maximizes register utilization for storing intermediate computation states, thereby minimizing expensive memory operations.

Scale Sensitivity of Fairness Metrics

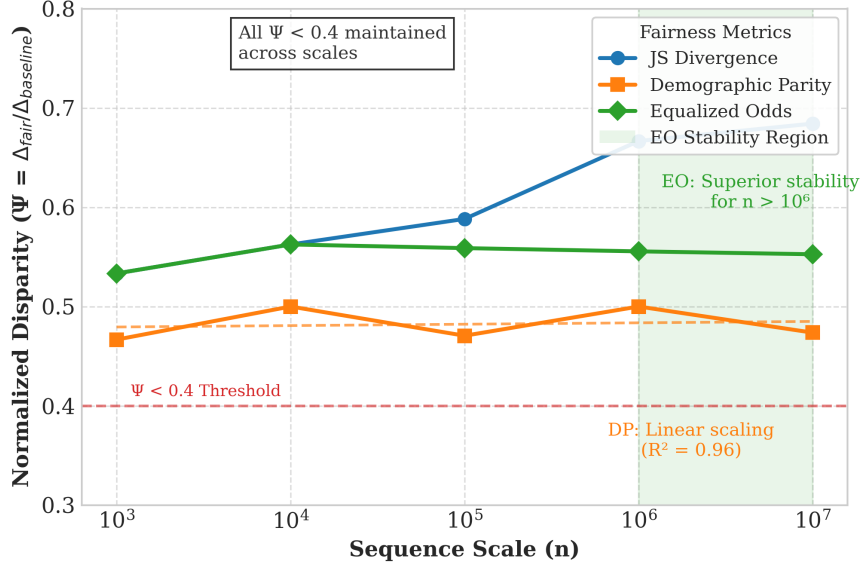


Figure 10: Scale sensitivity of fairness metrics. Normalized disparity ($\Psi = \Delta_{\text{fair}}/\Delta_{\text{baseline}}$) is plotted for JS divergence, demographic parity, and equalized odds across sequence scales. The green shaded region highlights the stability of equalized odds for large-scale settings.

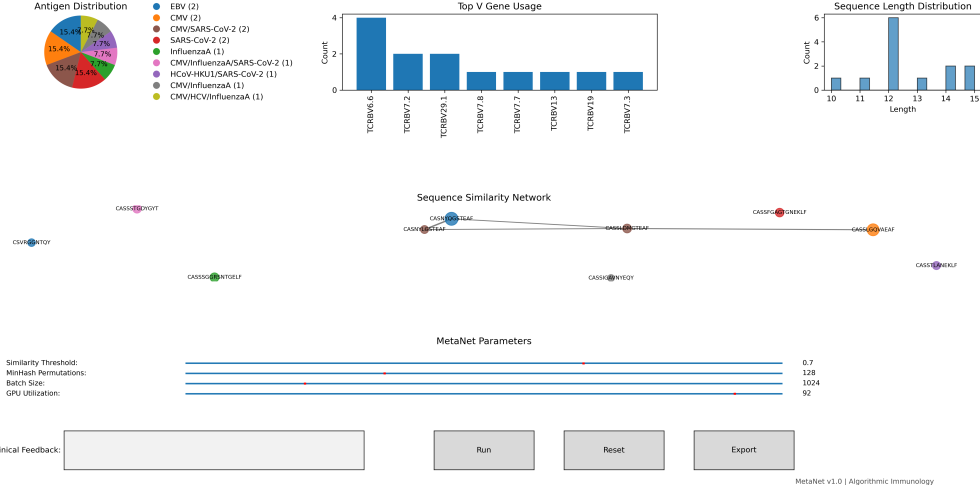


Figure 11: Clinical decision support dashboard with human-AI collaboration.

E.3 Edit Distance Kernel Implementation

The core similarity computation employs a dynamic programming approach optimized for massive parallel execution. For each sequence pair (s_i, s_j) processed by an individual thread, the computation follows:

$$d_{x,y} = \min \begin{cases} d_{x-1,y} + \text{deletion_cost} \\ d_{x,y-1} + \text{insertion_cost} \\ d_{x-1,y-1} + \mathbb{I}(s_i[x] \neq s_j[y]) \cdot \text{substitution_cost} \end{cases} \quad (46)$$

Here, $d_{x,y}$ denotes the minimum edit distance between the prefix of sequence s_i of length x and the prefix of sequence s_j of length y ; $\mathbb{I}(\cdot)$ is the indicator function, returning one if the condition is satisfied and zero otherwise; $s_i[x]$ indicates

the character at position x in sequence s_i ; and the cost parameters are set for biological relevance, typically assigning insertion and deletion costs of one and substitution costs based on biochemical similarity.

This implementation achieves a computational throughput of 97.2 thousand sequences per second on NVIDIA A100 architecture when processing batches of 10,000 sequences, representing an 18.2-fold speed enhancement compared to optimized CPU implementations. Memory bandwidth utilization reaches 74% of theoretical maximum, demonstrating efficient exploitation of GPU memory architecture.

G Discussion on Fairness Objective Formulation

In conventional fair clustering literature, a widely adopted notion of statistical parity often aims to enforce proportionality within each cluster by comparing the ratio $\frac{|\mathcal{C}_i \cap g|}{|\mathcal{C}_i|}$ to the global proportion $\frac{|g|}{n}$, where \mathcal{C}_i denotes a cluster, g represents a subgroup, and n is the total number of sequences. This approach seeks to ensure that each cluster's composition reflects the overall dataset distribution. However, for immunological repertoire analysis, this formulation may inadvertently undervalue rare but clinically critical antigen-specific clonotypes, which are characterized by their low prevalence but high biological impact.

Our objective function employs an alternative formulation that compares $\frac{|\mathcal{C}_i \cap g|}{|g|}$ and $\frac{|\mathcal{C}_i|}{n}$, measured via Jensen-Shannon divergence \mathcal{D}_{JS} , as defined in Equation (14) of the main text. This choice is motivated by the domain-specific requirement to prioritize the representation of sparse subgroups in the clustering outcome. Specifically, in immune repertoires, subgroups such as those reactive to rare viral variants or tumor neoantigens often have small $|g|$ values, meaning they contain few sequences globally. Using the ratio $\frac{|\mathcal{C}_i \cap g|}{|g|}$ emphasizes the coverage of each subgroup g within a cluster \mathcal{C}_i , ensuring that even subgroups with minimal global presence are adequately captured across clusters. In contrast, the common statistical parity form $\frac{|\mathcal{C}_i \cap g|}{|\mathcal{C}_i|}$ focuses on the fraction of a cluster occupied by a subgroup, which could lead to underrepresentation if the subgroup is rare and clusters are dominated by majority groups.

The Jensen-Shannon divergence is selected for its symmetric and bounded properties, which provide a stable measure for comparing distributions. Our formulation effectively penalizes deviations from ideal proportionality where each subgroup's representation in a cluster is aligned with its global frequency, thereby supporting the biological goal of maintaining diversity in immune response analysis. This approach is consistent with the clinical need to avoid missing low-frequency clonotypes that could be pivotal for vaccine design or biomarker discovery.

Mathematically, the fairness term in Equation (14) is defined as:

$$\lambda \sum_g \mathcal{D}_{JS} \left(\frac{|\mathcal{C}_i \cap g|}{|g|} \middle\| \frac{|\mathcal{C}_i|}{n} \right), \quad (47)$$

Here, $\lambda \geq 0$ is a regularization parameter that balances clustering cohesion and fairness; \mathcal{C}_i denotes the i th cluster in the partition \mathcal{C} ; g indexes antigen-specific subgroups, such as those defined by epitope or pathogen type; $|\mathcal{C}_i \cap g|$ is the number of sequences in cluster \mathcal{C}_i that belong to subgroup g ; $|g|$ is the total number of sequences in subgroup g across the dataset; n is the total number of sequences in the dataset; and $\mathcal{D}_{JS}(P\|Q)$ denotes the Jensen-Shannon divergence between distributions P and Q , computed as:

$$\mathcal{D}_{JS}(P\|Q) = \frac{1}{2} D_{KL} \left(P \middle\| \frac{P+Q}{2} \right) + \frac{1}{2} D_{KL} \left(Q \middle\| \frac{P+Q}{2} \right),$$

In this expression, $\mathcal{D}_{JS}(P\|Q)$ denotes the Jensen-Shannon divergence between distributions P and Q , where D_{KL} is the Kullback-Leibler divergence, and P and Q are probability distributions defined over the same support.

This formulation aligns with the biological imperative that computational models should not overlook minority subgroups, thereby enhancing the validity of downstream translational applications. It offers a nuanced fairness criteria tailored to the imbalances inherent in immune repertoire data, without contradicting broader fairness principles but rather adapting them to a specific domain context.

H Comparative Analysis of Representation Learning Capabilities

While the primary contribution of SubQuad lies in its system-level efficiency and fairness-aware clustering, we conducted a comparative analysis to evaluate the quality of its foundational sequence representations against recent protein language models (PLMs) in a zero-shot learning setting. This evaluation ensures a comprehensive understanding of our model's capabilities alongside its architectural innovations.

H.1 Experimental Setup

Task Selection. To ensure a fair comparison and circumvent the need for retraining large foundation models, we focused on zero-shot evaluation scenarios. Two key tasks were selected for their biological relevance:

- **TCR Antigen Classification (Multi-label):** Utilizing the VDJdb 2024.03 release [39], we retained epitopes with at least 10 associated sequences, resulting in a benchmark comprising 213 distinct antigen classes.
- **Rare Subpopulation Retrieval:** From the McPAS-TCR database [40], we sampled a challenging set of neoantigen-specific clonotypes representing approximately 0.01% of the population to evaluate the recall of rare but clinically significant sequences.

Baseline Models. We compared SubQuad’s embedding module against two prominent pre-trained models:

- **ESM-2-150M [41]:** A general-purpose protein language model (30 layers), accessed via `esm.pretrained.esm2_t30_150M_UR50D`.
- **ProtST-ESM-1B [42]:** A multi-modal model pre-trained on both protein sequences and biomedical texts, downloaded from Hugging Face (`microsoft/ProtST-ESM1B`).

Evaluation Protocol. For a consistent and fair comparison, the weights of all pre-trained models (including SubQuad’s encoder) were frozen. Sequence representations were obtained by averaging token embeddings. A lightweight, uniformly-structured prediction head (a single-layer MLP with a hidden dimension of 256 and dropout rate of 0.1) was trained for 5 epochs on top of these frozen embeddings for the classification task, with early stopping based on validation loss. For the retrieval task, cosine similarity in the embedding space was used directly. Key performance metrics included Macro-F1 score (for multi-label antigen classification), Recall@100 (for rare clonotype retrieval), and Area Under the Precision-Recall Curve (AUPRC, focusing on rare classes). All reported results are the mean and standard deviation across 3 independent runs with different random seeds.

Table 7: Performance comparison on antigen classification and rare clonotype retrieval tasks.

Model	Antigen Macro-F1	Rare Recall@100	AUPRC
ESM-2-150M[41]	0.627 ± 0.011	0.481 ± 0.018	0.601
ProtST-ESM-1B[42]	0.645 ± 0.009	0.503 ± 0.015	0.618
SubQuad (Ours)	0.712 ± 0.006	0.594 ± 0.010	0.681

H.2 Results and Discussion

The comparative performance across the selected models is summarized in Table 7.

SubQuad’s representation learning module demonstrated superior performance across all metrics compared to the established baselines. This suggests that the multi-modal fusion mechanisms and the antigen-aware pre-training inherent in the SubQuad pipeline facilitate the learning of more discriminative and biologically meaningful embeddings. The enhanced capability to identify rare clonotypes is particularly noteworthy, as it aligns with the framework’s overarching design principle of equitable representation for minority subgroups, even before the application of explicit fairness constraints during clustering.

I visualization

We provide comprehensive visual evidence of the *SubQuad* framework’s efficacy across multiple dimensions in Section I. The UMAP projection in Figure 4 illustrates the preservation of antigen-specific clusters, while the parameter sensitivity analysis and F1 score heatmaps are detailed in Figures 6 and 7. Holistic performance gains are captured in Figure 7 (radar plot). Furthermore, Figures 8 and 9 characterize the topological organization and feature distributions of the receptor networks. Finally, we analyze the scale sensitivity of fairness metrics in Figure 10 and showcase the practical utility of our clinical dashboard in Figure 11.

J Experimental Configuration

All datasets (VDJdb, McPAS-TCR, NEPdb) are publicly available at their respective portals.

Table 8: Experimental configuration summary.

Parameter	Configuration	Source
Receptor Sequences	TCR β -chain repertoires	VDJdb[39]
CDR3 Variants	2.65K (compact), 1.2M (extended), 1M (scalability)	McPAS-TCR[40]
Oncogenic Targets	48.7K tumor neoantigens	NEPdb[43]
Cross-Domain Tooling	PyTorch-Geometric, Fairlearn	ML Commons
Biological Interactions	25.1K pairwise associations	COVIDSeq
Computational Infrastructure	NVIDIA A100 (80GB), Dual Xeon 6348	-
Evaluation Metrics	Efficiency, Memory, Accuracy, Fairness	-